[AMERICAN JOURNAL OF SCIENCE, VOL. 295, JANUARY, 1995, P. 49–77]

ORIGIN OF FIBROSITY AND BANDING IN AGATES FROM FLOOD BASALTS

YIFENG WANG* and ENRIQUE MERINO
Department of Geological Sciences,
Indiana University, Bloomington, Indiana 47405

ABSTRACT. Agates are a remarkable case of textural and compositional self-organization, and their origin has far-reaching geochemical, crystal-growth, and petrologic implications. We conjecture that two mechanisms cooperate and interact during agate genesis: morphologically unstable crystallization fronts and cation-enhanced quartz growth. The model herein investigates the conditions under which these mechanisms work and their possible textural and chemical consequences. If a crystallization front is morphologically unstable (that is, if grad (growth rate) >0), then bumps on it lengthen into fingers, each finger generates others nearby, and all of them become a coherent fibrous texture with the fiber thickness set by the instability itself. Linear analysis of the morphological instability yields a dispersion equation that brings out factors favoring and impeding the generation of fibrous textures, and that for agates yields, as observed, "preferred" fiber thicknesses of a few micrometers.

Independently, if, as hypothesized, some cation(s) can enhance the rate of quartz growth then quartz growth becomes banded through

$$\text{Siliceous medium} \xrightarrow{c} \text{quartz} + H_2O + \text{cations},$$

where one of these released cations accelerates the reaction itself. The reaction produces oscillating silica and trace-element concentrations (and growth rates) at the inwardly advancing front. The fibers that grow (via the morphologically unstable front) through these concentration profiles are forced to take up oscillating amounts of Al or other traces for Si; this substitution causes the fibers to grow twisted and causes the twist period itself to oscillate also. Simultaneously, the oscillating concentrations at the front, through their effect on the morphological instability, cause the fiber thickness also to oscillate. The model thus predicts that quartz must crystallize in layers of fine, low-trace-element-content, untwisted fibers that repeatedly alternate with layers of finer, high-trace-element-content, twisted fibers. These associated predictions are precisely as observed, qualitatively and quantitatively.

SYMBOLS

c_c, c_s = "catalyst" and silica concentrations, mol/cm^3 (fig. 1)
c_c^0, c_s^0 = "catalyst" and silica concentrations at crystallization front
c_c^L, c_s^L = catalyst" "catalyst" and silica concentrations at $X = L^-$, just to the left of $X = L$ (fig. 1)
c_s^e = equilibrium silica concentration for a planar quartz growth front (eq 8)

* Present address: School of Earth and Atmospheric Sciences, Georgia Institute of Technology, Atlanta, Georgia 30332.

$c_s^{e'}$ = equilibrium silica concentration for a wavy quartz growth front (eq 6)
D_c, D_S = "catalyst" and polymeric-silica diffusion coefficients, cm^2/s
d_{ij} = integration constants (eqs B9-B10)
F = deviation of crystallization front from planar front (fig. 1)
f = scaled value of F (eqs 17)
G = growth rate of quartz, mol SiO_2/cm^2 s (eq 6)
$\overline{G}$ = average growth rate (eqs 7, A3)
g = scaled growth rate of quartz (eqs 13, 17)
$\overline{g}$ = scaled grwoth rate averaged over the crystallization front (eqs 17, 19C)
K = front curvature, defined by eq (9), in cm^{-1}
k = scaled front curvature (eqs 17)
L = thickness of boundary zone (fig. 1)
m = wave number, equal to $2\pi L/$(fiber thickness) (eq 40)
m_p = preferred wave number, corresponding to ζ_{max}
$\hat{n}$ = unit vector normal to the wavy front pointing out of quartz (eq 5)
s = scaled abscissa referred to the wavy front (eq 27)
t = time
u, v = scaled silica and "catalyst" concentrations (eqs 17)
$\overline{u}$, $\overline{v}$ = scaled silica and "catalyst" concentrations referred to the planar front
u^e = scaled quartz solubility c_s^e (eqs 17)
$\overline{u}^0$, $\overline{v}^0$ = scaled silica and "catalyst" concentrations at planar front
$\hat{u}$, $\hat{v}$, $\hat{g}$, $\hat{f}$ = amplitudes of perturbations δu, δv, δg, and δf respectively (eqs 40)
X, Y = spatial coordiates (fig. 1); X is distance from the planar front; Y coincides with the front
x, y = scaled values of X, Y (eqs 17)
α = scaled α' (eqs 17)
α' = rate constant, cm/s (eq 6)
β_1, β_2 = dimensionless positive constants to adjust cation-enhancing effect (eqs 12, 17)
β_1', β_2' = positive constants to adjust cation-enhancing effect (eq 6)
Γ = surface tension (cm) of quartz/water interface (eq 8)
γ = scaled surface tension, Γ/L (eqs 17)
δu, δv, δg, δf = small perturbations of u, v, g, f from their respective planar-front-referred values (eqs 34)
ϵ = ratio of silica concentration at $X = L^-$ to quartz molar density (eqs 17)
ζ = growth rate of perturbations from the planar front
η = moles of "catalyst" adsorbed on one mole of silica species (eq 4b)
θ = ratio of silica diffusivity to "catalyst" diffusivity
λ = scaled η (or adsorption strength) (eqs 17)

ρ = molar density of quartz (0.0445 mol/cm^3)
$\tau, \underline{\tau}', \tau''$ = scaled times (eqs 17, 21, 23)
∇, ∇^2 = gradient and Laplace operators

INTRODUCTION

Agates are rounded quartz bodies, 1 to 100 cm across, that occur in flood basalts. Most agates consist of concentric layers of length-fast fibrous chalcedony, an inner layer of coarse length-slow quartz crystals, and a central void. Strikingly, the fibers in *alternate* layers are *twisted*, very fine, and cathodo-luminescent, whereas the fibers in the intervening layers are untwisted, coarser, and non-luminescent. The repeated alternation of associated features, described by Merino (1984) and Wang and Merino (1990), is so striking and so self-similar in agates from different localities and ages, that their origin must be self-organizational (Nicolis and Prigogine, 1977; 1989)—that is, the oscillating textures and compositions must result from the internal dynamics of the growth itself, not from oscillating conditions outside the agate. Data on the twisting of the fibers (easily visible under the microscope and in fig. 6C below), their orientation, dislocations, structure, mineralogy, and on the trace elements, oxygen isotopes, occurrence, textures, and optical properties of agates, are given by Michel-Lévy and Munier-Chalmas (1892), Frondel (1962, 1978, 1985), Jones (1952), Correns and Nagelschmidt (1933), Raman and Jayaraman (1954), Florke and others (1982), Miehe, Graetsch, and Flörke (1984), Landmesser (1984), Fallick and others (1986), Harris (1989), Pankrath (1991), Heaney and Post (1992), Heaney (1993), Cady and others (1993), and many others.

What causes the systematic alternation in twisting and non-twisting of quartz fibers from layer to layer, and the associated alternation in fiber size, and the associated alternation in trace-element content (which we found initially by cathodo-luminescence,—Wang and Merino, 1990)? Why is the quartz fibrous? Why are the fine fibers of the concentric layers length-fast, but the coarse quartz of the innermost layer length-slow?[1] Why is the set of finely-crystalline fibrous layers systematically followed inward by a very-coarsely-crystalline, non-fibrous layer (and then a void)? We focus on these questions here; several more questions, petrological and crystal chemical, on the origin of agates are raised in Merino, Wang, and Deloule (1995b).

One idea of agate genesis is that agates form by precipitation of silica in voids within basalts (Frondel, 1962; Sunagawa and Ohta, 1976; Fallick and others, 1986); this idea implicitly assumes that the process requires transport of aqueous silica, and that it is an epigenetic, post-basalt, process—one unrelated to the igneous phenomenon represented by the basalt itself. Another idea of agate genesis is that agates form from

[1] In a length-fast quartz fiber the *c*-axis (which coincides with the 3-fold symmetry axis) is normal to the long dimension of the fiber. In a length-slow one the *c*-axis parallels the long dimension.

preëxisting, dense lumps of silica within basalts (Nacken, 1948; Liesegang, 1913), an idea that introduces the difficulty of accounting for the emplacement of those lumps in the first place (see discussion in Merino, 1984). A third idea combines elements of the previous two (Gonthier and others, 1988): first, filling of vesicles with siliceous aqueous solutions, then in-situ formation of a gel, and finally crystallization of the agate from that gel. Varied textural, isotopic, crystallographic, compositional, geological, and other evidence has been used to buttress one or another of these ideas, but the systematic agate textures and compositions we cite above, and in particular their association and alternation, have not been brought to bear on the question of agate genesis.

In the first article of this series (Wang and Merino, 1990), we proposed that the banding of agates is produced by quartz growth which was assumed to be accelerated by accumulation of cations at the growth front. We also proposed that fiber twisting is caused by trace-element substitution for Si^{4+}. The purpose of this paper is to produce a quantitative physicochemical model of the genesis of the agate's *fibrous texture* (which had been taken for granted in the earlier article) and of its interaction with the proposed banding mechanism and the solid-solution twisting mechanism. Our new hypothesis here is that fibrous textures of quartz in agates are the physical expression of crystallization fronts that were morphologically unstable. The instability spontaneously generates equally spaced fingers, each of which becomes a fiber, and whose assemblage becomes a fibrous texture. We first describe the morphological instability mechanism qualitatively, then develop a quantitative dynamic model of its interaction with the cation-enhanced growth, and then compare its predictions to observations. (This assumed cation-enhanced growth is modeled again below, both to integrate it quantitatively with the morphological instability and to correct our previous version, Wang and Merino, 1990. Below we often name this effect "catalysis" both for brevity and to indicate that we do not know through which mechanism rates are increased.)

In the third paper of the series (Merino, Wang, and Deloule, 1995a) we describe in detail interrelated geometric and crystal-chemical aspects of the new solid-solution fiber-twisting mechanism and give ion-probe trace-element profiles of agate quartz that confirm predictions of the general model.

The fibrous texture of agate quartz, the twisting of fibers, and the associated alternations in crystal size, twist period, and trace-element content, all turn out to be genetically interconnected and explained by our model. The model in addition predicts a host of other properties of agates (such as growth under closed-system conditions, inward decrease of ^{18}O content, occurrence of amethyst, association of zeolites with agates, Ni alteration of adjacent basalt, and others) which are confirmed by independent field, petrographic, and microanalytical evidence (Merino,

Wang, and Deloule, 1995a). If the hypothetical mechanisms incorporated herein into the quantitative agate-growth model become confirmed by additional work, the model will have unsuspected implications for crystal growth, the geochemistry and interpretation of crystalline textures, the behavior of basaltic magmas, and quartz polymorphism and crystal chemistry.

CRYSTALLIZATION OF AGATES

The system idealizing agate genesis is sketched in figure 1. An agate grows inwardly from its outer margin. The quartz crystallizes from a medium containing silica, cations, and water. We assume that the rate of

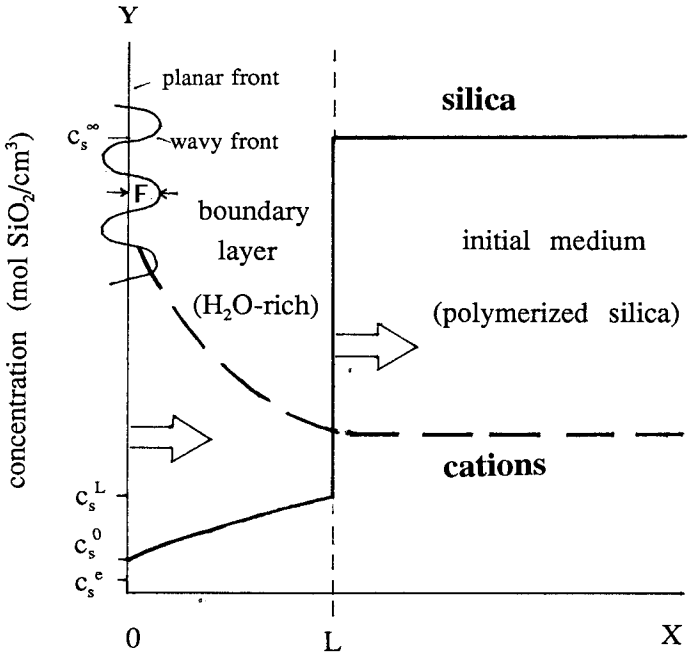

Fig. 1. Model system for agate crystallization with schematic profiles of silica concentration (moles SiO_2/cm^3) and trace-element concentration. The initial medium contains silica with attaced water and trace elements (such as Al, Na, K, Fe, and Ni, among others). Both distance along the front and concentrations are plotted vertically. Silica units travel to the crystallization front, where they build up quartz crystals and release the water and traces. Both water and traces accumulate at the front forming a silica-depleted boundary layer of thickness L. One or more of the traces is assumed to enhance quartz growth. The crystallization front advances to the right. It becomes morphologically unstable and develops fingers, which become quartz fibers. The c_s values shown vertically are silica concentrations in the initial medium ($^\infty$), at $X = L^-$ just inside the right side of the boundary layer, at the planar front (^{0}), and at equilibrium with a planar quartz surface (^{e}), respectively. We suppose that $c_s^L/\rho < 0.2$ (ρ = quartz molar density).

quartz growth can be enhanced by cations.[2] For agate growth, we also assume that these cations are carried to the growth front by whatever silica species exist in the system. As silica becomes incorporated into quartz, the accumulation of the rate-enhancing cation (= "catalyst") at the front accelerates further quartz growth, which in turn, by the reaction

$$\text{Silica polymers} \xrightarrow{c} \text{quartz} + \text{cations} + H_2O, \qquad (1)$$

releases even more "catalyst." The growth rate becomes so high that silica becomes depleted in the boundary layer. This depletion greatly slows down growth and gives time for the "catalyst" to diffuse (inwardly) away from the front and for silica to diffuse to the front. As silica recovers, so does the growth rate of quartz; "catalyst" resumes accumulating at the front and accelerates growth, bringing in a new spurt. This positive feedback causes the concentrations of silica and "catalyst" at the crystallization front to be oscillatory, and this is confirmed quantitatively below.

Our assumption above that cations are carried to the front attached to the silica species is easy to satisfy if the silica were polymeric, which would be likely if the system were sufficiently rich in silica. The implication that the medium is rich in silica is consistent with (1) the growth of fibrous spherulites from silicate melts (Lofgren, 1980); (2) the fact that quartz fibers in agate are length-fast, an optical orientation probably produced by the attachment of silica chains flat onto the growing crystal surface (Folk and Pittman, 1971); and (3) the experimental production of fibrous chalcedony from dense silica gels by White and Corwin (1961) and Oehler (1976). Because heat diffuses fast over the small size of agates, relative to their growth rate, their crystallization (which is exothermic) cannot appreciably modify the local temperature and is taken here as isothermal.

FIBROSITY PRODUCED BY FRONT INSTABILITY

We also assume that the fibrous texture of agate is the physical expression of a morphologically unstable crystallization front. A similar cause of fibrosity in organic polymers was proposed by Keith and Padden (1963, 1964). A surface is morphologically unstable if any small deviation from planarity tends to grow, rather than dampen, as time goes on. Thus, a morphologically unstable crystallization front requires that the gradient of growth rate away from the front be positive:

$$\left.\frac{d\bar{G}}{dX}\right|_{X=0} > 0, \qquad (2)$$

[2] Experimental hints supporting our assumption that some cations may accelerate quartz (or silica) growth can be found in Campbell and Fyfe (1960) for Na^+; Halperin, Schieber, and Braner (1970) for Mg^{2+}, Na^+, Ga^{3+}, V^{5+}, and Zn^{2+}; Mitsyuk (174) for K^+; Kastner, Keene, and Gieskes (1977, p. 1055) for Mg^{2+}, Al^{3+}, Fe^{3+}, and Mn^{2+}; and Hosaka and Taki (1981a,b,c) for Na^+ and K^+. Iler (1973, p. 12-13) reports that alkalis can help quartz grow from silica sols. In addition, quartz crystals are routinely grown faster from Na^+-bearing baths.

where $\overline{G}$ represents the growth rate of quartz, and X is the distance away from the planar front (fig. 1). If eq (2) is satisfied, any incipient bump on the quartz crystallization front spontaneously should become longer (but with length limited by surface tension), quickly depleting its immediately surrounding region of its silica (region dashed in fig. 2). This precludes quartz from growing at regions "a," next to the initial bump. Quartz can now grow only far enough from "a," at regions (labelled "b") unaffected by the depletion. The front advances at "b," leaving the "a" regions behind. Now the "b" regions themselves become new bumps and evolve just as the original one did. Thus, even just one initial bump on an unstable front will grow into a finger and generate others around itself, and these others, and so on. The front may have many initial bumps. Each of them should do what the one in figure 2A does, as explained above. Where two adjacent ones are close enough to each other, they compete for silica, and they raise the local surface energy, and one of them must therefore become stunted or disappear. After this "weeding" is completed, the spacing between remaining fingers (= fiber thickness) becomes independent of the initial distribution of bumps. The result is a bundle of parallel quartz fibers—a fibrous texture.

Eq (2) directly links the morphological instability of the front to the kinetics of cation-enhanced quartz growth through reaction (1). We show below that the joint operation of the two mechanisms produces the association of repetitive textures and compositions found routinely in agates.

QUANTITATIVE MODEL

Continuity equations.—We place the Y axis to coincide with the planar front, defined as the planar average of the wavy agate crystallization front, as shown in figure 1. The actual wavy shape of the front at any time t is described by $X = F(Y, t)$, which is the horizontal deviation from the planar average front. Both mass transfer across the boundary zone and growth at the front must satisfy mass continuity:

for $X > F(Y, t)$:

$$\frac{\partial c_s}{\partial t} = D_s \nabla^2 c_s \tag{3A}$$

$$\frac{\partial c_c}{\partial t} = D_c \nabla^2 c_c \tag{3B}$$

at $X = F(Y, t)$:

$$G = D_s \vec{\nabla} c_s \cdot \vec{n} \tag{4A}$$

$$0 = D_c \vec{\nabla} c_c \cdot \vec{n} + \eta G \tag{4B}$$

at $X = L$:

$$c_s = c_s^L, \quad c_c = c_c^L \tag{4C}$$

where c_s and c_c are concentrations of silica and catalyst respectively; D_s and D_c are diffusion coefficients of silica and catalyst respectively; L is the thickness of the boundary zone; c_i^L is c_i evaluated at $X = L^-$, that is, slightly to the left of L; G is the rate of reaction (1); η is moles of catalyst

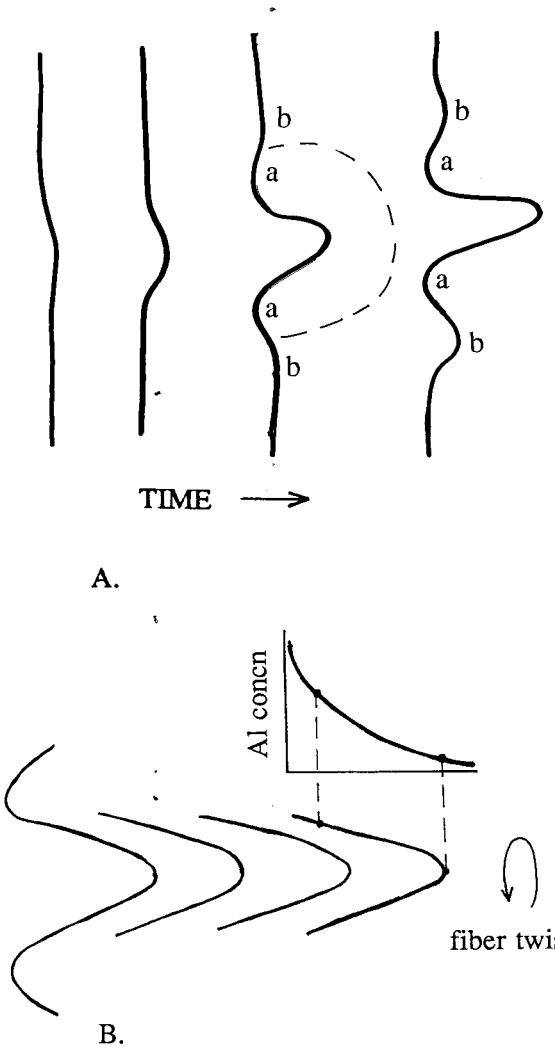

Fig. 2(A). Successive stages of a morphologically unstable crystallization front. If the instability condition, grad(growth rate) > 0, is satisfied, any bump on the front becomes longer *and* produces other fingers next to itself, and these produce others, generating a fibrous texture. The region "a" is depleted in silica because of the fast growth of the finger—see text. (B) Each quartz fiber grows by addition of conical sleeves. As each sleeve pierces through a decreasing trace-element concentration profile (dashed in fig. 1), its rim is forced to take up a higher trace-element content than its tip. The rim-to-core Al^{3+} gradient thus forced into each fiber makes the fiber grow twisted because Al-O bonds are longer than Si-O bonds.

adsorbed on one mole of silica species; and $\vec{n}$ is the unit normal vector on the wavy front pointing toward the agate's center, defined by

$$\vec{n} = \left(1, -\frac{\partial F}{\partial Y}\right)^T \Big/ \left[1 + \left(\frac{\partial F}{\partial Y}\right)^2\right]^{1/2}. \tag{5}$$

Reaction rate.—Following the general form of rate laws (Aagaard and Helgeson, 1982, eq 1) we take the rate of reaction (1) to grow with increasing "catalyst" concentration, and we assume it grows linearly with the affinity of reaction (= silica concentration at the front minus the equilibrium concentration; see Rimstidt and Barnes, 1980). In addition, since we deduce independently (for reasons given in the Introduction, Merino 1984; Wang and Merino 1990) that agate textures must be self-organizational, and since self-organization requires nonlinearity (Nicolis and Prigogine, 1977, p. 90-94), we also assume here that the rate is nonlinear for "catalysis:"

$$G = \alpha'[1 + \beta_1'(c_c^0) + \beta_2'(c_c^0)^2](c_s^0 - c_s^{e'}) \tag{6}$$

where c_i^0 are concentrations (of "catalyst" c and silica s) at the front; $c_s^{e'}$ is an equilibrium silica concentration; α' is a rate constant; and β_1' and β_2' are positive constants that describe the strength of the rate-enhancing effect. Eq (6) contains "1 +" inside the "catalytic" factor to preclude the rate from vanishing for zero catalyst, an algebraic detail we think should be added to the general laws proposed by Aagaard and Helgeson (1982) and Nagy and Lasaga (1992). (Note also that eq 6 can be regarded as a truncated Taylor's expansion of a monotonic increasing function of quartz growth rate with "catalyst" concentration.)

Front advance kinematics.—The reaction rate, G, is related to the advance of the front, $\partial F/\partial t$, by the folowing kinematic equation (see app. A):

$$G\left[1 + \left(\frac{\partial F}{\partial Y}\right)^2\right]^{1/2} - \overline{G} = \rho \frac{\partial F}{\partial t} \tag{7}$$

where $\overline{G}$ is average growth rate, ρ is molar density of quartz, and F is the deviation of the wavy front from its planar average. Eq (7) follows from the fact that the front advances only because quartz grows; the front advance is an aspect of the growth.

Surface tension.—Variations in the shape and curvature of the front modify the surface energy associated with it. This is why the equilibrium silica concentration that appears in eq (6) depends on the surface tension and the curvature, according to (Cheronov and Nishinaga, 1987; Chadam and Ortoleva, 1983),

$$c_s^{e'} = c_s^e(1 + \Gamma K) \tag{8}$$

where c_s^e is the equilibrium silica concentration for a planar quartz surface, Γ characterizes the surface tension of the quartz/initial-medium interface,[3] and K is surface curvature, defined by

$$K = -\frac{\partial^2 F}{\partial Y^2} \Big/ \left[1 + \left(\frac{\partial F}{\partial Y}\right)^2\right]. \tag{9}$$

Surface tension obviously must oppose growth and lengthening of front fingers, because this raises the specific surface.

Dimensionless equations.—Eqs (3-9) form a closed system that describes both the morphological and the cation-enhanced-quartz-growth instabilities, as well as their interaction. They can be cast into the following scaled and dimensionless form:

for $x > f(y, \tau)$,

$$\frac{\partial u}{\partial \tau} = \nabla^2 u \tag{10A}$$

$$\theta \frac{\partial v}{\partial \tau} = \nabla^2 v \tag{10B}$$

at $x = f(y, \tau)$,

$$g = \vec{\nabla} u \cdot \vec{n} \tag{11A}$$

$$0 = \vec{\nabla} v \cdot \vec{n} + \lambda g \tag{11B}$$

$$g = \alpha(1 + \beta_1 v + \beta_2 v^2)[u - u^e(1 + \gamma k)] \tag{12}$$

$$g\left[1 + \left(\frac{\partial f}{\partial y}\right)^2\right]^{1/2} - \bar{g} = \frac{1}{\epsilon}\frac{\partial f}{\partial \tau} \tag{13}$$

$$\vec{n} = \left(1, -\frac{\partial f}{\partial y}\right)^T \Big/ \left[1 + \left(\frac{\partial f}{\partial y}\right)^2\right]^{1/2} \tag{14}$$

$$k = -\frac{\partial^2 f}{\partial y^2} \Big/ \left[1 + \left(\frac{\partial f}{\partial y}\right)^2\right]^{3/2} \tag{15}$$

at $x = 1$,

$$u = 1, \quad v = 0 \tag{16}$$

[3] The length Γ is related to the standard surface energy through $\Gamma = 2v\sigma/RT$ (derived from eq (5-14) in Berner, 1980), where v is molar volume of quartz, σ is the interfacial free energy of quartz/water interface (350 mJ/m^2 from Parks, 1984), R is the gas constant, and T is absolute temperature.

where

$$x = \frac{X}{L}, \quad y = \frac{Y}{L}, \quad \tau = \frac{L^2}{D_s}t,$$

$$u = \frac{c_s}{c_s^L}, \quad v = \frac{(c_c - c_c^L)}{c_c^L}, \quad u^e = \frac{c_s^e}{c_s^L},$$

$$\theta = \frac{D_s}{D_c}, \quad \alpha = \frac{L\alpha'[1 + \beta_1'(c_c^L) + \beta_2'(c_c^L)^2]}{D_s},$$

$$\beta_1 = \frac{\beta_1'(c_c^L) + 2\beta_2'(c_c^L)^2}{1 + \beta_1'(c_c^L) + \beta_2'(c_c^L)^2}, \quad \beta_2 = \frac{\beta_2'(c_c^L)^2}{1 + \beta_1'(c_c^L) + \beta_2'(c_c^L)^2}$$

$$\lambda = \frac{D_s c_s^L}{D_c c_c^L}\eta, \quad \gamma = \frac{\Gamma}{L}, \quad k = KL, \quad f = \frac{F}{L},$$

$$\epsilon = \frac{c_s^L}{\rho}, \quad g = \frac{L}{D_s c_s^L}G, \quad \bar{g} = \frac{L}{D_s c_s^L}\bar{G}. \tag{17}$$

General strategy.—To investigate the tendency to fingering (that is, the instability) of the agate crystallization front, we need first to find the solution to eqs (10-16) with respect to the planar front; this first stage of the model thus focuses on the genesis of the agate banding. The second stage is to impose small perturbations on the planar-front solution in order to study whether they tend to grow or become flattened with time.

REPETITIVE BANDING: PLANAR-FRONT SOLUTION

The planar-front solution is governed by the following equations, which are obtained by making f and all derivatives with respect to y equal to 0 in eqs (10-16):

for $x > 0$,

$$\frac{\partial \bar{u}}{\partial \tau} = \frac{\partial^2 \bar{u}}{\partial x^2} \tag{18A}$$

$$\theta \frac{\partial \bar{v}}{\partial \tau} = \frac{\partial^2 \bar{v}}{\partial x^2} \tag{18B}$$

at $x = 0$,

$$\bar{g} = \frac{\partial \bar{u}}{\partial x} \tag{19A}$$

$$0 = \frac{\partial \bar{v}}{\partial x} + \lambda \bar{g} \tag{19B}$$

$$\bar{g} = \alpha(1 + \beta_1 \bar{v} + \beta_2 \bar{v}^2)(\bar{u} - u^e) \tag{19C}$$

at x = 1,

$$\bar{u} = 1, \quad \bar{v} = 0 \tag{19D}$$

where $\bar{u}$, $\bar{v}$ and $\bar{g}$ are the u, v, and g referred to the planar front. By integrating both sides of eq (18) over $0 \leq x \leq 1$, using the approximations

$$\int_0^1 \bar{u}dx \approx \frac{1 + \bar{u}^0}{2}, \quad \int_0^1 \bar{v}dx \approx \frac{\bar{v}^0}{2} \tag{20A}$$

$$\left.\frac{\partial \bar{u}}{\partial x}\right|_{x=1} \approx 1 - \bar{u}^0, \quad \left.\frac{\partial \bar{v}}{\partial x}\right|_{x=1} \approx -\bar{v}^0, \tag{20B}$$

and introducing a new time scale

$$\tau' = 2\tau, \tag{21}$$

one obtains

$$\frac{d\bar{u}^0}{d\tau'} = 1 - \bar{u}^0 - \alpha(1 + \beta_1\bar{v}^0 + \beta_2\bar{v}^{02})\bar{u}^0$$

$$\theta\frac{d\bar{v}^0}{d\tau'} = -\bar{v}^0 + \lambda\alpha(1 + \beta_1\bar{v}^0 + \beta_2\bar{v}^{02})\bar{u}^0 \tag{22}$$

where $\bar{u}^0$, $\bar{v}^0$ are scaled silica and "catalyst" concentrations at the planar front, respectively. Presumably being very small compared to u^0, u^e is neglected in deriving eqs (22). Eqs (22) turn out to be formally identical to those derived for trace-element zoning in calcite (Wang and Merino, 1992). We adapt here our results for that problem. Linear instability analysis of the equations (Cook, 1986) shows that the system displays different behaviors around different steady states (see app. in Wang and Merino, 1992, for details) and provides ranges of parameter values for which the system of eqs (22) can have oscillatory solutions. Figure 3 shows the behaviors of the system for a given set of values for some parameters. One sees for example that the concentrations can oscillate if the ratio of diffusivities of silica to "catalyst" is $\theta = D_s/D_c < 1$, since a greater ratio would place the system in the region of no oscillations. For agates to acquire *many* repetitive bands, as they often do, the behavior should be of the constant-amplitude type, because this type allows many turns around the steady state, whereas the other types only allow a few turns before the system "falls" onto a steady state. The condition for the constant-amplitude oscillations is that $\theta < 0.2$, or that silica have a very low diffusivity. This internal condition of the model suggests therefore that the initial medium should be dense and polymerized,[4] since polymerized-

[4] As indeed happens in the crystallization experiments of Lofgren (1980) and the experimental production of fibrous chalcedony from dense silica gels by White and Corwin (1961) and Oehler (1976).

silica molecules would indeed have much lower diffusivity in the boundary-layer than "catalyst" cations would.

The full non-linear system (22), when solved numerically (by backward finite differences) for values of α, λ, β_1, β_2, and θ that satisfy the linear instability analysis, indeed yields oscillatory solutions. As shown below, the oscillations produce the typical repetitive bands displayed by agates.

Because this banding model arises from the general system of eqs (10-16) (which was not true of the banding model proposed in Wang and Merino, 1990), it is automatically consistent with the study of the front's morphological instability presented below. Both banding models, however, provide similar estimates of the spacing between bands and the time needed for the crystallization of each band. For the purpose of illustration, for the solutions shown in figure 4, and arbitrarily taking $D_s \sim 10^{-7}$ cm^2/s and $L \sim 0.1$ cm, we obtain that the time to form one band is about 30 hrs and that the corresponding spacing of bands is about 0.1 mm. This value is within one order of magnitude of observed agate-band spacings.

The concentrations of trace elements other than the "catalyst" should oscillate also and in phase with the "catalyst" concentration. Because of the mass-action law, the content of each trace element that enters the quartz fibers should be proportional to the corresponding concentration at the front and should therefore oscillate from band to band also. This prediction is confirmed for Fe, Al, Na, K, and H by ion- and electron-probe microanalysis (Merino, Wang, and Deloule, 1995a) and by cathodoluminescence (Wang and Merino, 1990).

DUAL TIME SCALES: BANDING AND FIBROSITY

Eq (13) gives the relation between g, the growth rate relative to the actual wavy front, and $\bar{g}$, the growth rate relative to the planar front, as a function of f, the horizontal separation between the two fronts; f is a function of y and τ. Note that by defining a new time, τ'', such that

$$\tau'' = \epsilon\tau, \tag{23}$$

all terms in eq (13) become of order one, implying that τ'' is the time scale on which front fingering evolves and on which it should be studied. From eqs (21, 23) one obtains

$$\tau'' = \frac{\epsilon}{2}\tau'. \tag{24}$$

ϵ equals the ratio of silica concentration just left of the retreating front (fig. 1) to the density of quartz. As hypothesized above, the silica concentration in the water-rich boundary layer should be substantially lower than in the initial medium—though still much higher than quartz saturation in H_2O, which, at, say, 800°C and 1 kb, is 0.1 moles silica/kg water (Walther and Helgeson, 1977). Thus, *if* we chose $\epsilon = 0.2$, we would deduce from eq (24) that front fingering happens ten times faster than

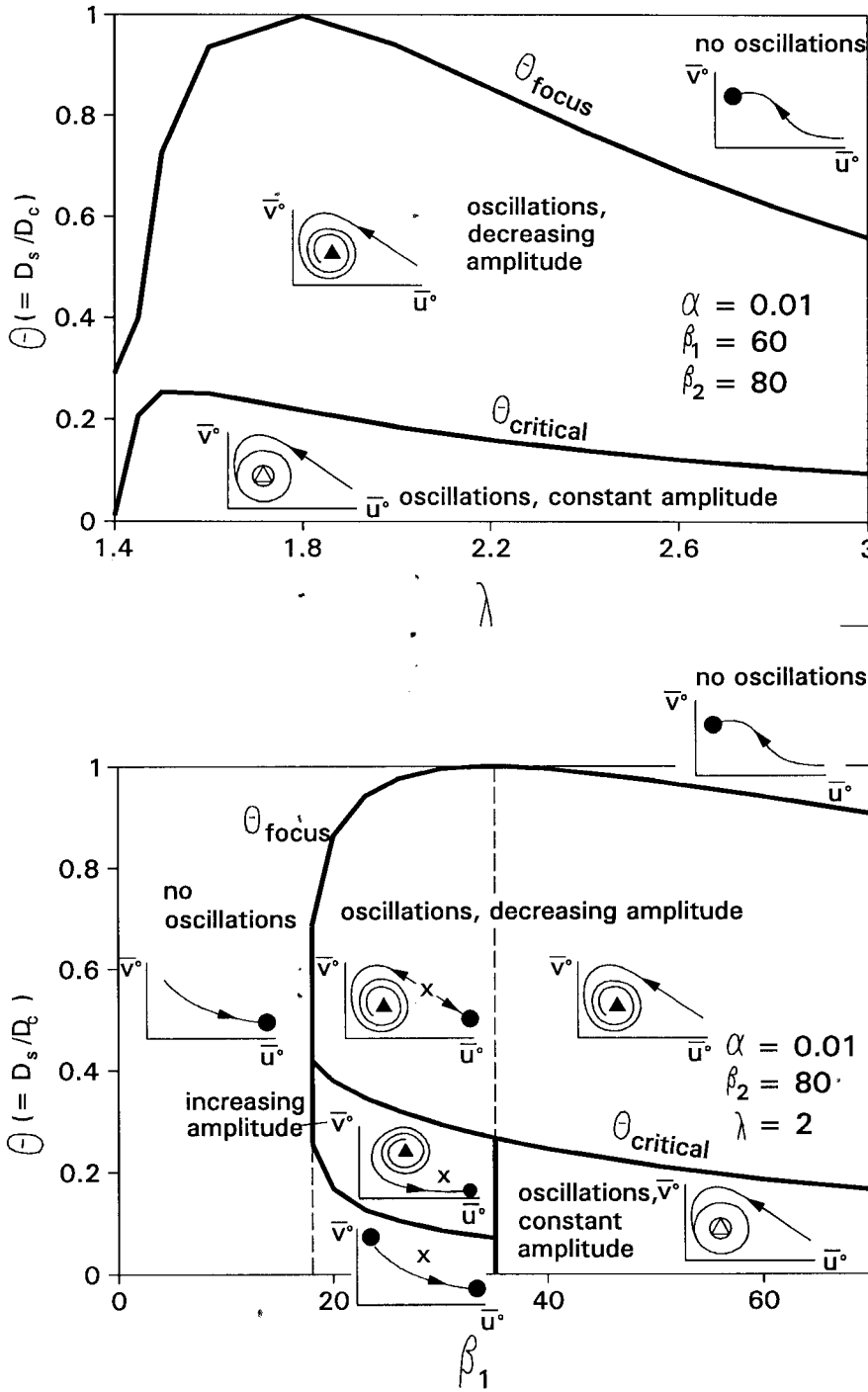
no oscillations
Θ_{focus}
oscillations, decreasing amplitude
α = 0.01
β_1 = 60
β_2 = 80
$\Theta_{critical}$
oscillations, constant amplitude
Θ (= D_s/D_c)
λ
no oscillations
Θ_{focus}
no oscillations
oscillations, decreasing amplitude
increasing amplitude
α = 0.01
β_2 = 80
λ = 2
$\Theta_{critical}$
oscillations, constant amplitude
Θ (= D_s/D_c)
β_1

Fig. 3

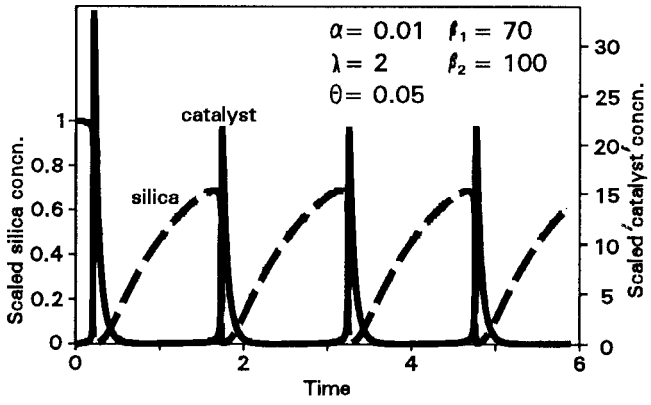

Fig. 4 Scaled silica and "catalyst" concentrations at the planar front versus scaled time τ', calculated with eqs (22), for the parameter values shown. The oscillations in the two concentrations are produced by the cation-enhanced reaction (1). Quartz growth rate, obtained entering the concentrations shown at any one time into eq (19C), also turns out to be temporally oscillatory but is not shown.

banding. This difference in time scales, in turn, would justify taking $\bar{u}$ and $\bar{v}$, silica and "catalyst" concentrations referred to the planar front, as essentially constant on the time scale of fingering (that is, fibrosity). This is the choice we make below to facilitate the morphological instability analysis that follows.

With eq (23), eqs (10, 13) become

for $x > f(y, \tau'')$,

$$\epsilon \frac{\partial u}{\partial \tau''} = \nabla^2 u$$

$$\epsilon\theta \frac{\partial v}{\partial \tau''} = \nabla^2 v \tag{25}$$

$$g\left[1 + \left(\frac{\partial f}{\partial y}\right)^2\right]^{1/2} - \bar{g} = \frac{\partial f}{\partial \tau''}. \tag{26}$$

Fig. 3. Behavior diagrams for agate banding, in parameter space, indicating four types of concentration oscillations, along with ranges of parameters for each type. Each behavior type applies over a labelled field defined by solid curves, which are obtained by linear analysis and numerical simulation. These diagrams are identical to those found for oscillatory calcite crystallization—see figure 6 and appendix in Wang and Merino (1992) for the meaning of various types of steady states symbolized by crosses, circles, and triangles and for meaning of the $\theta_{critical}$ and θ_{focus} curves, which are calculated with eqs (A9-10) in Wang and Merino (1992). In particular, below the $\theta_{critical}$ curve the system is unstable around the steady state, here meaning that the silica and "catalyst" concentrations spontaneously cycle around the steady state (if there is only one steady state). A "focus" (solid triangles) is a steady state that the system oscillatorily approaches or deviates from. Since agates normally display *many* repetitive bands, the banding should be of the constant-amplitude type (lower right), which requires θ to remain below about 0.2, which in turn requires $D_{silica} \ll D_{"catalyst"}$, which is consistent with the silica being polymerized.

LINEAR ANALYSIS OF MORPHOLOGICAL INSTABILITY

The aim of this analysis is to see whether small departures from the planar-front solution to eqs (10-16) increase (instability) or decrease (stability) as time passes. The procedure for linear analysis is given for example in Sekerka (1973), Nicolis and Prigogine (1989, p. 241-255), Ortoleva and others (1987, p. 1025 and following), and Tritton (1988, p. 251-258). We first transform the coordinate system from (x, y, τ'') to (s, y, τ'') with

$$s = x - f(y, \tau''). \tag{27}$$

In the new coordinate system eqs (11, 12, 14-16, 25, 26) become

for $s > 0$,

$$\left[1 + \left(\frac{\partial f}{\partial y}\right)^2\right]\frac{\partial^2 u}{\partial s^2} + \frac{\partial^2 u}{\partial y^2} - 2\frac{\partial^2 u}{\partial y \partial s}\frac{\partial f}{\partial y} - \frac{\partial u}{\partial s}\frac{\partial^2 f}{\partial y^2} = \epsilon\frac{\partial u}{\partial \tau''}$$

$$\left[1 + \left(\frac{\partial f}{\partial y}\right)^2\right]\frac{\partial^2 v}{\partial s^2} + \frac{\partial^2 v}{\partial y^2} - 2\frac{\partial^2 v}{\partial y \partial s}\frac{\partial f}{\partial y} - \frac{\partial v}{\partial s}\frac{\partial^2 f}{\partial y^2} = \theta\epsilon\frac{\partial v}{\partial \tau''} \tag{28}$$

at $s = 0$,

$$g = \left[\frac{\partial u}{\partial s} - \frac{\partial f}{\partial y}\left(\frac{\partial u}{\partial y} - \frac{\partial u}{\partial s}\frac{\partial f}{\partial y}\right)\right]\Bigg/\left[1 + \left(\frac{\partial f}{\partial y}\right)^2\right]^{1/2}$$

$$-\lambda g = \left[\frac{\partial v}{\partial s} - \frac{\partial f}{\partial y}\left(\frac{\partial v}{\partial y} - \frac{\partial v}{\partial s}\frac{\partial f}{\partial y}\right)\right]\Bigg/\left[1 + \left(\frac{\partial f}{\partial y}\right)^2\right]^{1/2} \tag{29}$$

$$g = \alpha(1 + \beta_1 v + \beta_2 v^2)[u - u^e(1 + \gamma k)] \tag{30}$$

$$k = -\frac{\partial^2 f}{\partial y^2}\Bigg/\left[1 + \left(\frac{\partial f}{\partial y}\right)^2\right]^{3/2} \tag{31}$$

$$g\left[1 + \left(\frac{\partial f}{\partial y}\right)^2\right]^{1/2} - \bar{g} = \frac{\partial f}{\partial \tau''}. \tag{32}$$

At $s = 1 - f$,

$$u = 1, \quad v = 0. \tag{33}$$

We now introduce small departures into the equations by writing each relevant variable as the sum of the corresponding value referred to the planar front plus a deviation from it:

$$\begin{aligned} u &= \bar{u}(s, y, \tau'') + \delta u(s, y, \tau'') \\ v &= \bar{v}(s, y, \tau'') + \delta v(s, y, \tau'') \\ g &= \bar{g}(y, \tau'') + \delta g(y, \tau'') \\ f &= \delta f(y, \tau''). \end{aligned} \tag{34}$$

Inserting eqs (34) into eqs (28-33), collecting linear terms in δu, δv, δg, and δf, and neglecting terms quadratic or higher in the deviations (this is why this analysis is called "linear"), one obtains a set of linearized equations:

for $s > 0$,

$$\frac{\partial^2 \delta u}{\partial s^2} + \frac{\partial^2 \delta u}{\partial y^2} - \frac{d\bar{u}}{ds}\frac{\partial^2 \delta f}{dy^2} = \epsilon \frac{\partial \delta u}{\partial \tau''}$$

$$\frac{\partial^2 \delta v}{\partial s^2} + \frac{\partial^2 \delta v}{\partial y^2} - \frac{d\bar{v}}{ds}\frac{\partial^2 \delta f}{dy^2} = \epsilon\theta \frac{\partial \delta v}{\partial \tau''} \qquad (35)$$

at $s = 0$,

$$\delta g = \frac{\partial \delta u}{\partial s}$$

$$-\lambda \delta g = \frac{\partial \delta v}{\partial s} \qquad (36)$$

$$\delta g = \frac{\partial \bar{g}}{\partial \bar{u}}\left(\delta u + u^e \gamma \frac{\partial^2 \delta f}{\partial y^2}\right) + \frac{\partial \bar{g}}{\partial \bar{v}} \delta v \qquad (37)$$

$$\delta g = \frac{\partial \delta f}{\partial \tau''} \qquad (38)$$

and at $s = 1$

$$\delta u = \frac{d\bar{u}}{ds} \delta f$$

$$\delta v = \frac{d\bar{v}}{ds} \delta f. \qquad (39)$$

Now the unknowns are the departures themselves. By the method of separation of variables (Crank, 1975) it can be seen that the solutions to the linearized system have the form

$$\begin{aligned} \delta u &= \hat{u}(s) e^{\zeta \tau''} \cos(my) \\ \delta v &= \hat{v}(s) e^{\zeta \tau''} \cos(my) \\ \delta g &= \hat{g} e^{\zeta \tau''} \cos(my) \\ \delta f &= \hat{f} e^{\zeta \tau''} \cos(my), \end{aligned} \qquad (40)$$

where the quantities under the $\hat{}$ are the amplitudes of δu, δv, δg, and δf; ζ is the growth rate of deviations; and m is the wave number of the

sinusoidal deviation. Following app. B, one obtains

$$\zeta = \frac{\left.\frac{d\bar{u}}{ds}\right|_{s=0}\left(m\frac{d\bar{g}}{ds} - u^e\gamma m^3\frac{\partial\bar{g}}{\partial\bar{u}}\right)}{m\left.\frac{d\bar{u}}{ds}\right|_{s=0} + \frac{e^{2m}-1}{e^{2m}+1}\frac{d\bar{g}}{ds}}, \tag{41}$$

where $\partial\bar{g}/\partial\bar{u}$, $\partial\bar{g}/\partial\bar{v}$, and $d\bar{g}/ds$ are related to $\bar{u}^0$ and $\bar{v}^0$ in eqs (22)—the planar banding model—by

$$\frac{\partial\bar{g}}{\partial\bar{u}} = \alpha(1 + \beta_1\bar{v}^0 + \beta_2\bar{v}^{02})$$

$$\frac{\partial\bar{g}}{\partial\bar{v}} = \alpha(\beta_1 + 2\beta_2\bar{v}^0)(\bar{u}^0 - u^e)$$

$$\frac{d\bar{g}}{ds} = \frac{\partial\bar{g}}{\partial\bar{u}}\left.\frac{d\bar{u}}{ds}\right|_{s=0} + \frac{\partial\bar{g}}{\partial\bar{v}}\left.\frac{d\bar{v}}{ds}\right|_{s=0}$$

$$\approx \frac{\partial\bar{g}}{\partial\bar{u}}(1 - \bar{u}^0) - \frac{\partial\bar{g}}{\partial\bar{v}}\bar{v}^0. \tag{42}$$

PHYSICAL INTERPRETATION OF EQ (41)

Eq (41) can be viewed as a dispersion equation, as it gives velocity as a function of wavelength. It characterizes whether the crystallization front is morphologically stable ($\zeta < 0$ for all $m > 0$: deviations in eq 40 attenuate with time) or unstable ($\zeta > 0$ for some m: deviations grow) and yields predictions of the preferred spacing between fibers. Eq (41) brings out the physicochemical factors favoring and impeding the generation of a fibrous texture.

For $d\bar{g}/ds > 0$ (that is, for greater growth rates at the tips of bumps than at their bases), which is the necessary condition for instability of the front (see eq 2), the denominator of eq (41) must be positive, and then the sign of ζ coincides with the sign of the numerator in eq (41). The positive term in this numerator is then the driving force for instability, and the negative term is the resisting, or stabilizing, force. This must be correct, because physically the surface tension must indeed *resist* production of fibers, which increases the surface area. Mineral solubility, represented by u^e, also is seen to work against the generation of fibers. Instability is helped by high-enough $d\bar{g}/ds$, which means (eq 42) high growth-rate constant, α, and strong rate enhancement, though this is not necessary, because zero beta coefficients still would not preclude α from being high enough. In particular, for the diffusion-limited case ($\alpha \to \infty$) with no "catalyst" ($\bar{v}^0 = 0$), eq (41) yields an expression for m_p identical to that found independently by Cheronov and Nishinaga (1987, eq 81). In agate crystallization, therefore, the essential role of quartz growth rate-enhancement by cations is to make concentrations at the front oscillate;

this oscillation makes the fiber thickness oscillate also, as explored in the next section. To apply eqs (41, 42), which are general, to other cases, we need only find appropriate expressions for the growth rate $\bar{g}$.

For $d\bar{g}/ds > 0$ the front should be morphologically stable, as expressed by eq (2). This coincides with what eq (41) says, since it yields negative ζ values. (Eq 41 yields positive ζ values for $m > 2$, a range far outside the range of interest. This conflict between eqs (2) and (41) may arise simply from dropping the small right-hand terms in eqs (35), as justified in app. B.)

Selection of preferred fiber spacing.—A plot of ζ versus m is shown in figure 5. ζ must maximize for a high enough m, denoted as m_p in figure 5, because of the m^3 in the second term of the numerator in eq (41). Of all the possible perturbation wavelengths in the natural crystallization front, we expect the one with wavenumber m_p to establish itself the fastest, because its growth rate is maximum. Thus, the fiber spacing adopted by the system should be $2\pi L/m_p$. For $\gamma = 0.64 \times 10^{-5}$ (see footnote 3) and $L = 0.1$ cm, the preferred fiber spacing is 5 μm, which falls in the range of observed agate quartz fiber thicknesses. (For the case where $dg/ds < 0$ and to avoid the inconsistency in eq (41) pointed out above, we have assigned $m_p = 0$ in fig. 7B, meaning that the planar front, that is, the perturbation with infinite wavelength, is preferred.)

ASSOCIATED OSCILLATING FIBER THICKNESS AND TRACE ELEMENT CONTENT

Eqs (41-42) show that the morphological instability depends on the planar-front concentrations $\bar{u}^0$ and $\bar{v}^0$, which oscillate in time, as shown in

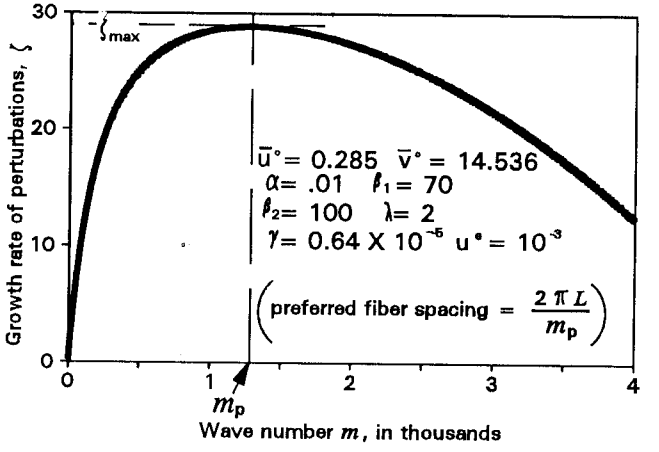

Fig. 5. Growth rate of morphological perturbations of the crystallization front versus their wave number m (= $2\pi L$/spacing), from eq (41) using indicated parameter values. The values for $\bar{u}^0$ and $\bar{v}^0$ are chosen to fall on the limit-cycles of figure 7A and B. For the parameters chosen, ζ is positive (which means the front is morphologically unstable thus becoming fibrous) and maximizes for a certain m, m_p. The fiber spacing "preferred" and adopted by the system thus is $2\pi L/m_p$.

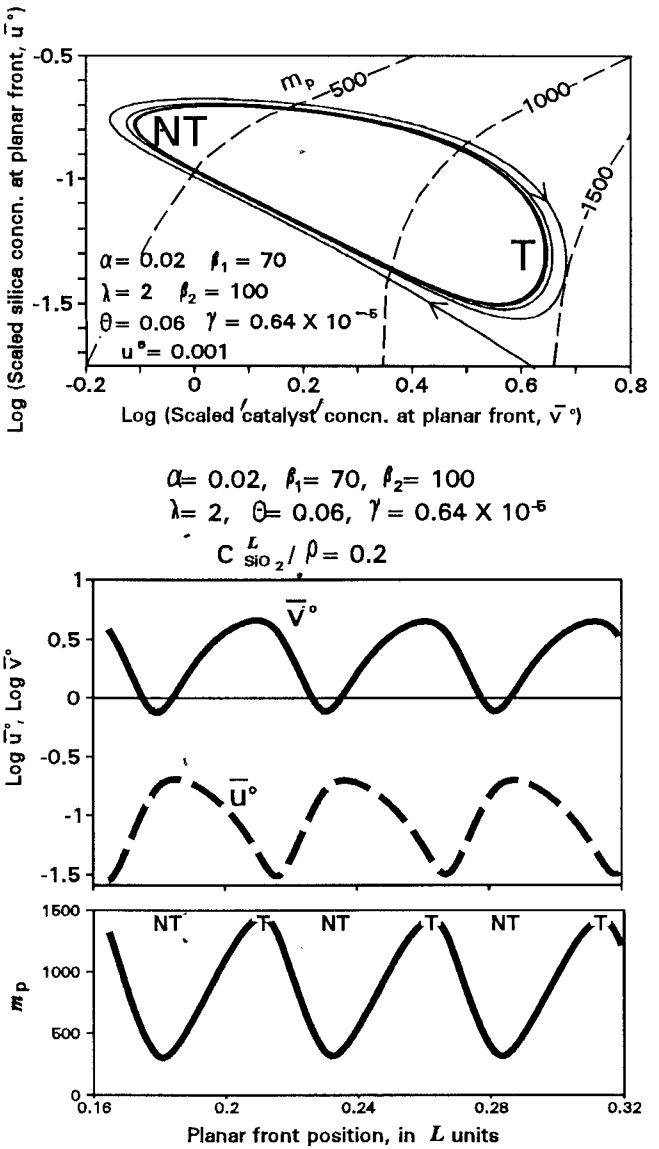

Fig. 6(A) Limit-cycle (corresponding to the constant-amplitude region in fig. 3) showing the linked oscillations in silica and catalyst concentrations at the planar front and their evolution (arrows) for the indicated parameter values. The limit cycle is obtained by numerical solution of the planar-front dynamic equations—see text and Wang and Merino (1992). Superimposed on the cycle are contours of m_p, the preferred wave number, calculated from eq (41) as in figure 5. As concentrations cycle around the loop, the preferred fiber spacing repeatedly increases along the bottom of the cycle and decreases along its top; thus, silica and cation concentration oscillations are linked to oscillating fiber thicknesses, as observed in frame C.

(B) Same information in (A) is shown here versus position of the planar front. T means twisted fiber and is produced by high cation concentrations $\bar{v}^0$ and can be seen to coincide with small fiber thickness. NT means fiber is little (or not) twisted, because $\bar{v}^0$ is lowest, and coincides with the thickest fibers.

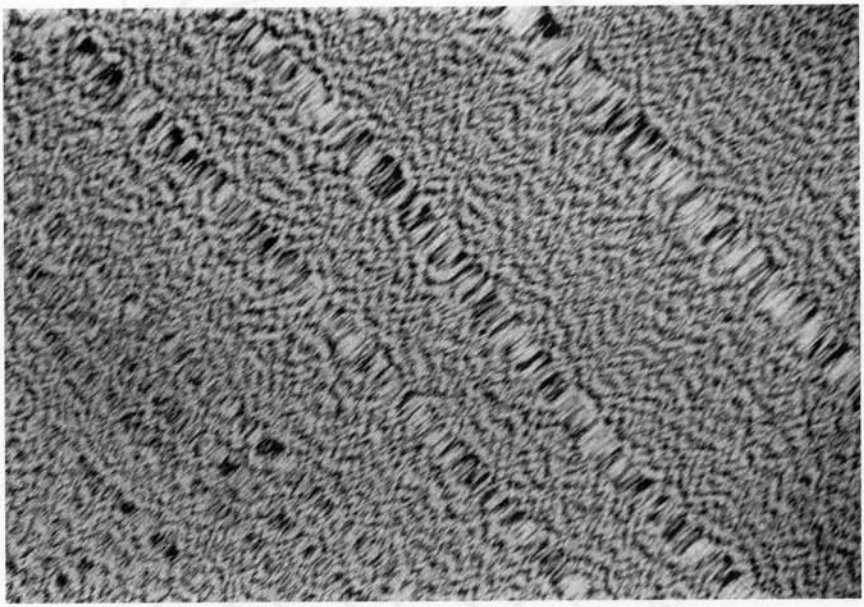

Fig. 6(C) Photomicrograph of a portion of an agate exactly displaying the predictions made in frames (A, B): association of very fine fibers with tight twisting and (from ion-probe analyses reported in Merino, Wang, and Deloule, 1995a), with highest Al and K contents.

figure 4. Hence, the fiber thickness also must oscillate during agate crystallization. For example, in figure 6A we show contours of m_p in the ($\log \overline{u}^0$, $\log \overline{v}^0$) plane; these contours are obtained by finding from eq (41) the m_p for each possible pair of $\overline{u}^0$, $\overline{v}^0$ values and for given values of α, β_1, and β_2. Also shown is one closed trajectory (a "limit cycle") of oscillatory planar-front concentrations obtained from eqs (22) for the same values of α, β_1, and β_2 used to calculate m_p plus particular values of λ and θ. The intersections of the contours with the closed cycle represent the values of the preferred fiber spacing along the cycle. As the system repeatedly cycles (see arrows) along the closed trajectory, the preferred fiber spacing is seen to oscillate also. The associated values of $\overline{u}^0$, $\overline{v}^0$, and m_p in figure 6A are also shown in figure 6B versus front position. Figure 6A and B thus predicts that crystallization would proceed in layers of fine fibers alternating with layers of less fine (4 times thicker) fibers. Just an occurrence of this sequence, common in agates, is shown in figure 6C.

In contrast, in figure 7A we show a case (for the same parameter values used in figure 6A except that α and θ are now slightly lower) in which the $m = 0$ contour happens to cross the closed cycle of concentrations, $\overline{u}^0$ and $\overline{v}^0$. This implies that as the system cycles along the closed trajectory (see arrows) it repeatedly goes into and out of morphological instability. This is also shown in figure 7B versus front position. In this

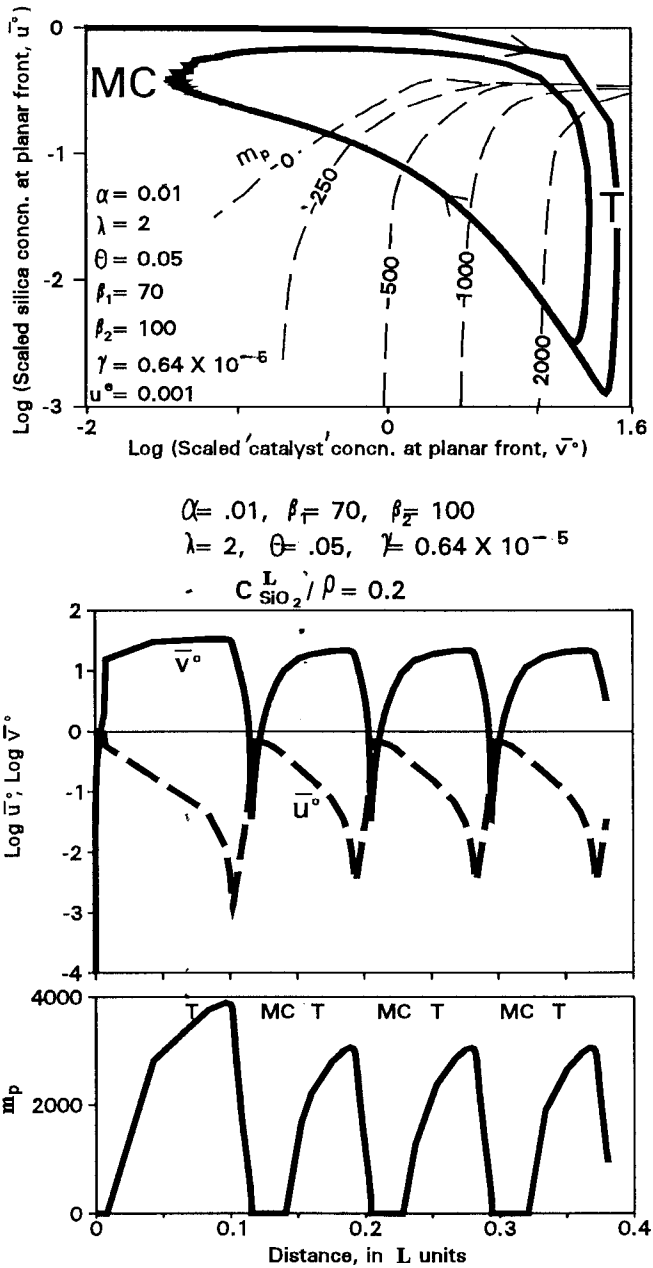

Fig. 7(A) Another case of limit-cycle behavior, also producing constant-amplitude variations in silica and "catalyst" concentrations at the growth front. Parameter values are slightly different from those used for figure 6A. Superimposed on the cycle are contours of m_p, the reciprocal of the preferred fiber spacing. Here, unlike in figure 6A, the $m_p = 0$ contour intersects the concentration cycle, indicating that the system goes repeatedly into and out of morphological instability, alternatively yielding (twisted) fibers, T, and microcrystalline, equant quartz, MC. (B) Same information shown in (A), but here versus the planar-front coordinate measured from the starting position at the outer edge of the agate. On the m_p curve are shown the regions where crystals are predicted to be tightly twisted fibers (T) and regions where the quartz is predicted to be *not* fibrous but microcrystalline (MC).

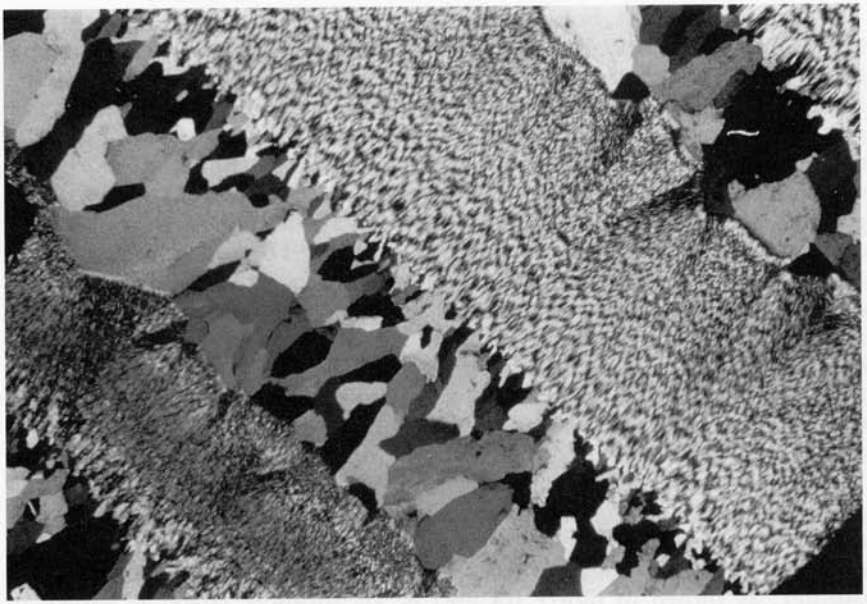

Fig. 7(C) Same agate of figure 6C here showing a repeated sequence of textures exactly as predicted in frames (A, B) above: layers of fibrous crystals alternating with layers of non-fibrous (microcrystalline) crystals.

case crystallization is predicted to proceed in layers of fine fibers that alternate with layers of *non-fibrous* crystals. An example of this alternation, from the same agate of figure 6C, is shown in figure 7C.

Figures 6B and 7B display the correspondence between fiber size and "catalyst" concentration at the front. Recalling that high values of "catalyst" concentration at the front, $\overline{v}^0$, cause high trace-element contents to be incorporated in quartz (see end of section on Repetitive Banding above), it follows that the finer fibers should incorporate higher trace-element contents. This is exactly as observed by petrography and cathodo-luminescence (Wang and Merino, 1990) and by ion-probe microanalyses (Merino, Wang, and Deloule, 1995a). The incorporation of one or more of these trace elements, in particular Al^{3+}, causes fibers to grow twisted, as discussed next.

FIBER TWISTING: TRACE-ELEMENT DISTRIBUTION IN EACH FIBER

We proposed that agate fiber twisting is caused by Al substitution for Si (Wang and Merino, 1990). A corrected quantitative model of this mechanism, along with microanalytical evidence for it, is given in Merino, Wang and Deloule (1995a). Here we show quantitatively that substitutional twisting of agate fibers is directly produced by the joint action of the morphological instability and cation-enhanced growth modeled above.

We suppose that, because fiber thickness is imposed by the morphological instability and because the fingers must be essentially conical, fibers grow by accretion of conical sleeves (fig. 2B), as in Langer (1980). Simultaneously, as the fingered crystallization front advances, trace elements (including the catalyst) accumulate ahead of it, developing negative concentration gradients away from the front (fig. 1). The conical sleeves of quartz, as they grow through these decreasing concentration profiles, are therefore forced to incorporate a higher trace element content at their bases than at their tips (fig. 2B). The final fiber inevitably ends up being richer in trace elements in its periphery than along its center. As shown by microanalysis (Merino, Wang, and Deloule, 1995a), at least one of these traces, Al^{3+}, and probably also Fe^{3+}, oscillatorily enters the quartz fibers in substitution for Si.[5] The need for the fiber to maintain its structural continuity while simultaneously making room for the larger (and more abundant) Al^{3+} ions along its periphery requires that it grow twisted[6] in proportion to the fiber's rim-to-core Al gradient.[7] This gradient increases with increasing $\bar{v}^0$, for two reasons: First, as $\bar{v}^0$ goes up, the trace-element-concentration *gradient* ahead of the front also increases, forcing a greater difference in incorporated trace content from center to periphery of each fiber. And second, the fiber itself becomes thinner, as shown in figure 6A and B. In addition, since, as shown in figures 4 and 6B, $\bar{v}^0$ oscillates, so does the twist period. The thinnest fibers are therefore predicted to be the richest in trace elements and the most tightly twisted, and the thicker fibers are predicted to be poorer in trace elements and less twisted. These predictions of twisting are added as labels T and NT (or MC) in figures 6B and 7B. Examples of these predictions are shown in figures 6C and 7C and in Merino, Wang, and Deloule (1995b).

CONCLUSIONS

We give a comprehensive dynamic model of agate crystallization and agate textures and composition. The model is based on the hypotheses that the quartz growth rate is enhanced by cations and that fibrous textures are produced by the spontaneous fingering of morphologically unstable crystallization fronts. The model takes account of mass continuity, diffusion, reaction kinetics, and the shape and surface energy of the moving crystallization front. Because the crystallization of agate is self-organizational and because self-organization requires non-linearity (Nico-

[5] Al-for-Si substitution is also shown by Flörke and others (1982, fig. 8) for whole-agate compositions and, among others, by Pankrath (1991) and references therein for synthetic quartz.

[6] This mechanism is similar to one proposed by Keith and Padden (1961) for polymeric organic compounds.

[7] The close connection among quartz growth rate, aluminum incorporation by quartz, and defects has been experimentally studied by Brown and Thomas (1960), Martin and Armington (1983), and many others for industrial applications to the growth of synthetic quartz. It makes sense to hypothesize that the abundant defects detected in agate quartz by Cady and others (1993) and Heaney (1993) are produced by annealing of the twisting produced by the incorporation of trace elements.

lis and Prigogine, 1977, p 90-94), the growth rate of quartz is assumed to be non-linear in the cation concentration. Crystallization from an unspecified medium containing water, cations, and silica starts at the margin of the agate and proceeds inward. As quartz grows, the "catalyst" cation(s) segregated just ahead of the advancing front accelerate quartz growth—and hence their own further accumulation. This feedback causes the silica and trace element concentrations at the front to oscillate.

Simultaneously, the front becomes morphologically unstable: incipient bumps on the crystallization surface grow longer and become fingers. Each bump, precisely because it is the locus of fast growth, must give rise to other bumps near it, just beyond a minimum distance. The condition for morphological instability is that the growth rate at the tips of bumps be greater than at their bases. Since the growth rate depends on cation concentration, fingering of the front becomes linked to the enhancement of quartz growth by cations, reaction (1). The time scale of repetitive banding turns out to be larger than the time scale of front fingering.

Each finger becomes a crystal fiber by accretion of conical sleeves of quartz. As each conical sleeve of quartz forms, it crosses the decreasing trace-element concentration profiles produced by the cation "auto-enhancement" of quartz growth rate. As a result, the rim of the sleeve is forced to incorporate a higher content of trace elements than its tip is. Thus, the fiber formed by aggregation of many sleeves becomes righer in trace elements along its periphery than along its center. Ion-probe analyses (Merino, Wang, and Deloule, 1994a,b) indicate that Al is one of these traces, and that it enters the quartz fibers in substitution for Si. AlO bonds being longer than SiO bonds, the fiber is forced to grow twisted to accommodate the larger peripheral Al content.

By linear instability analysis, the model produces a dispersion equation (eq 41) that brings out the factors that promote (high growth rate constant and rate enhancement by cations) and those that impede (surface tension and solubility) morphological instability of the crystallization front. Eq (41) also allows us to calculate the preferred fiber spacing (and thickness) adopted by the system in a particular case. Eq (41) links the genesis of fibrosity and the preferred fiber spacing to the oscillations in silica and trace-element concentrations produced by quartz growth rate enhancement by cations accumulated at the front. That linkage is responsible for the simultaneous oscillations of fiber sizes, fiber twist period, and trace element concentrations predicted by the model, a prediction that matches observations remarkably well.

Because the model is so successful in predicting a very stringent association of textures and compositions, we think its ideas and mechanisms have widespread implications (some of which are discussed in Merino, Wang, and Deloule, 1995b) for the geochemistry of crystalline textures, crystal growth, the crystal chemistry and polymorphism of quartz, and the origin of agates.

ACKNOWLEDGMENTS

We thank the NSF Division of Earth Sciences for support through grants EAR-9003633 and EAR-9104198. We thank Jonathan Foise (Sawyer Research Products, Inc., East Lake, Ohio) for discussion and information on cation-enhancement of quartz growth rates, José Escobar (Mathematics, Indiana University) for discussion on linear instability analysis, and Patricia Dove (Georgia Tech) and Lorie Canada (Bloomington) for help. We appreciate perceptive critical comments by William Murphy (Southwest Research Institute, San Antonio), an anonymous reviewer, D. Rye as editor, and especially the associate editor and Phillipe Van Cappellen (Georgia Tech). Their comments and criticism have immeasurably helped us improve the manuscript. Roy Young (of Nature's Own, Nederland, Colorado) and Brian Jackson (of the Royal Museum of Scotland, Edinburgh) generously gave us many Brazilian and Scottish agate samples.

APPENDIX A

In the X, Y system (with Y coinciding with the planar crystallization front, fig. 1), the front is described by

$$X - F(Y, t) = 0, \tag{A1}$$

where F(Y, t) is the deviation from the average position of the front. Taking derivatives with respect to time t, one obtains

$$\frac{\partial X}{\partial t} - \frac{\partial F}{\partial Y}\frac{\partial Y}{\partial t} - \frac{\partial F}{\partial t} = 0. \tag{A2}$$

The growth rate is related to $\partial X/\partial t$ and $\partial Y/\partial t$ by

$$\frac{G\vec{n}}{\rho} = \frac{1}{\rho}\begin{pmatrix}\overline{G}\\ 0\end{pmatrix} + \begin{pmatrix}\dfrac{\partial X}{\partial t}\\ \dfrac{\partial Y}{\partial t}\end{pmatrix}, \tag{A3}$$

where the velocity of advance at each point of the wavy front (left side) is split into the advance velocity of the planar front plus the deviation velocity of the wavy relative to the planar front. $\vec{n}$ is the unit normal vector defined by eq (5); $\overline{G}$ is the growth rate of the planar (or average) front; and ρ is molar density of quartz. Combining eqs (A2–A3) and eq (5) and eliminating $\partial X/\partial t$ and $\partial Y/\partial t$, one obtains eq (7). This derivation parallels that given by Ortoleva and others (1987, eq VI.8 and app. B) for the kinematics of motion of the reaction front.

APPENDIX B

In the section on linear analysis of the morphological instability, and because banding takes place ten times faster than fibrosity, we have made the simplification that $\overline{u}$, $\overline{v}$ are at steady state on the time scale of fibrosity, τ''. Also, we may neglect the right sides of eqs (35) because ϵ is probably small (= 0.2—see section on dual time scales), and, at any rate,

because, to avoid uninteresting transients, the derivatives $\partial\delta u/\partial\tau''$ and $\partial\delta v/\partial\tau''$ themselves are neglected. (Sekerka, 1973, made a similar simplification in a similar case of morphological instability.) Inserting eqs (40) into eqs (35–39), we obtain

for $s > 0$,

$$\frac{d^2\hat{u}}{ds^2} - m^2\hat{u} + \frac{d\bar{u}}{ds} m^2\hat{f} = 0 \tag{B1}$$

$$\frac{d^2\hat{v}}{ds^2} - m^2\hat{v} + \frac{d\bar{u}}{ds} m^2\hat{f} = 0; \tag{B2}$$

at $s = 0$,

$$\hat{g} = \frac{d\hat{u}}{ds} \tag{B3}$$

$$-\lambda\hat{g} = \frac{d\hat{v}}{ds} \tag{B4}$$

$$\hat{g} = \frac{\partial\bar{g}}{\partial\bar{u}}(\hat{u} - u^e\gamma m^2\hat{f}) + \frac{\partial\bar{g}}{\partial\bar{v}}\hat{v} \tag{B5}$$

$$\hat{g} = \zeta\hat{f}; \tag{B6}$$

at $s = 1$,

$$\hat{u} = \frac{d\bar{u}}{ds}\hat{f} \tag{B7}$$

$$\hat{v} = \frac{d\bar{v}}{ds}\hat{f}. \tag{B8}$$

The solutions to eqs (B1-B2) are of the form

$$\hat{u} = d_{11}e^{ms} + d_{12}e^{-ms} + \frac{d\bar{u}}{ds}\hat{f} \tag{B9}$$

$$\hat{v} = d_{21}e^{ms} + d_{22}e^{-ms} + \frac{d\bar{v}}{ds}\hat{f}, \tag{B10}$$

where d_{ij} is a constant. Incorporating boundary conditions (B3-B4, B7-B8) into eqs (B9–B10) and using eq (B6), we obtain

at $s = 0$,

$$\hat{u} = \left[-\frac{e^{2m} - 1}{m(e^{2m} - 1)}\zeta + \frac{d\bar{u}}{ds}\right]\hat{f} \tag{B11}$$

$$\hat{v} = \left[\frac{\lambda(e^{2m} - 1)}{m(e^{2m} + 1)}\zeta + \frac{d\bar{v}}{ds}\right]\hat{f} \tag{B12}$$

$$\zeta\hat{f} = \frac{\partial\bar{g}}{\partial\bar{u}}(\hat{u} - u^e\gamma m^2\hat{f}) + \frac{\partial\bar{g}}{\partial\bar{v}}\hat{v}. \tag{B13}$$

For the above equations to have nontrivial solutions for $\hat{u}$, $\hat{v}$ and $\hat{f}$, the determinant of the coefficient matrix for $\hat{u}$, $\hat{v}$ and $\hat{f}$ must be zero, which gives rise to eq (41) in the text.

References

Aagaard, P., and Helgeson, H. C., 1982, Thermodynamic and kinetic constraints on reaction rates among minerals and aqueous solutions. I. Theoretical considerations: American Journal of Science, v. 282, p. 237–285.

Berner, R. A., 1980, Early Diagenesis: A Theoretical Approach: Princeton, New Jersey, Princeton University, 241 p.

Brown, C. S., and Thomas, L. A., 1960, The effect of impurities on the growth of synthetic quartz: Journal of Physics and Chemistry of Solids, v. 13, p. 337–343.

Cady, S. L., Wenk, H.-R., Kilaas, R., and Barber, D. J., 1993, Enantiomorphism and planar defects in length-fast chalcedony, *in* Boland, J. N., and Fitz Gerald, J. D., editors, Defects and Processes in the Solid State, Geoscience Applications. The McLaren Volume: Amsterdam and New York, Elsevier, p. 383–400.

Campbell, A. S., and Fyfe, W. S., 1960, Hydroxyl-ion catalysis of the hydrothermal crystallization of amorphous silica; a possible high temperature pH indicator: American Mineralogist, v. 45, p. 464–468.

Chadam, J., and Ortoleva, P., 1983, The stabilizing effect of surface tension on the development of the free boundary in a planar, one-dimensional, Cauchy-Stefan problem: Journal of Applied Mathematics, v. 30, p. 57–66.

Cheronov, A. A., and Nishinaga, T., 1987, Growth shapes and their stability at anisotropic interface kinetics: Theoretical aspects for solution growth, *in* Sunagawa, I., editor, Morphology of Crystals: Part A: Boston, Reidel, p. 207–267.

Cook, P. A., 1986, Nonlinear Dynamical Systems: Englewood Cliffs, New Jersey, Prentice-Hall, 216 p.

Correns, C. W., and Nagelschmidt G., 1933, Über Faserbau und optische Eigenschaften von Chalzedon: Zeitschrift für Kristallographie, v. 85, p. 199–213.

Crank, J., 1975, The Mathematics of Diffusion: Oxford, Clarendon Press, 414 p.

Fallick, A. E., Jocelyn, J., Donnelly, T., Guy, M., and Behan, C., 1985, Origin of agates in volcanic rocks from Scotland: Nature, v. 313, p. 672–674.

Flörke, O. W., Köhler-Herbertz, B., Langer, K., and Tönges, I., 1982, Water in microcrystalline quartz of volcanic origin agates: Contributions to Mineralogy and Petrology, v. 80, p. 324–333.

Folk, R. L., and Pittman, J. S., 1971, Length-slow chalcedony: A new testament for vanished evaporites: Journal of Sedimentary Petrology, v. 41, p. 1045–1058.

Frondel, C., 1962, Silica Minerals; Dana's System of Mineralogy, v. 3: New York, Wiley, 334 p.

———— 1978, Character of quartz fibers: American Mineralogist, v. 63, p. 17–27.

———— 1985, Systematic compositional zoning in the quartz fibers of agates: American Mineralogist, v. 70, p. 975–979.

Gonthier, E., Skrok, J., Apter, M., and Fröhlich, F., 1988, L'univers des agates: Revue de Gemmologie (special issue for an exhibit at the National Museum of Natural History, 36 rue Geoffroy Saint-Hilaire, 75005 Paris), 12 p.

Halperin, A., Schieber, M., and Braner, A. A., 1970, Radiation effects on quartz crystals and oscillators, and growth of doped quartz crystals: Report by Hebrew University, Physics Department, sponsored by Air Force Cambridge Research Laboratories through the European Office of Aerospace Research, U.S. Air Force, under Contract F 61052-69-C-0015, 45 p.

Harris, C., 1989, Oxygen-isotope zonation of agates from Karoo volcanics of Skeleton Coast, Namibia: American Mineralogist, v. 74, p. 476–481.

Heaney, P. J., 1993, A proposed model for the crystallization of chalcedony: Contributions to Mineralogy and Petrology, v. 115, p. 66–75.

Heaney, P. J., and Post, J. E., 1992, The widespread distribution of a novel silica polymorph in microcrystalline quartz varieties: Science, v. 255, p. 441–443.

Hosaka, M., and Taki, S., 1981a, Hydrothermal growth of quartz crystals in NaCl solutions: Journal of Crystal Growth, v. 52, p. 837–842.

———— 1991b, Hydrothermal growth of quartz crystals in KCl solutions: Journal of Crystal Growth, v. 53, p. 542–546.

———— 1981c, Hydrothermal growth of quartz crystals in pure water: Journal of Crystal Growth, v. 51, p. 640–642.

Iler, R. K., 1973, Colloidal silica, *in* Matijević, E., editor, Surface and Colloid Science: volume 6: New York, Wiley, p. 1–100.

Jones, F. T., 1952, Iris agate: American Mineralogist, v. 37, p. 578–587.

Kastner, M., Keene, J. B., and Gieskes, J. M., 1977, Diagenesis of siliceous oozes, I. Chemical controls on the rate of opal-A to opal-CT transformation—an experimental study: Geochimica et Cosmochimica Acta, v. 41, p. 1041–1059.

Keith, H. D., and Padden, F. J., Jr., 1961, Note on the origin of twisting orientation in fibrillar crystals: Journal of Polymer Science, v. 51 (156), p. S4–S7.
———— 1963, A phenomenological theory of spherulitic crystallization: Journal of Applied Physics, v. 34, p. 2409–2421.
———— 1964, Spherulitic crystallization from the melt. I. Fractionation and impurity segregation and their influence on crystalline morphology: Journal of Applied Physics, v. 35, p. 1270–1285.
Landmesser, M., 1984, Das Problem der Achatgenese: Mitteilungen der Pollichia, v. 72, p. 5–137.
Langer, J. S., 1980, Instabilities and pattern formation: Reviews of Modern Physics, v. 52, p. 1–28.
Liesegang, R. E., 1913, Geologische Diffusionen: Dresden, Steinkopff, 180 p.
Lofgren, G., 1980, Experimental studies on the dynamic crystallization of silicate melts, *in* Hargraves, R. B., editor, Physics of Magmatic Processes: Princeton, New Jersey, Princeton University, p. 487–551.
Martin, J. J., and Armington, A. F., 1983, Effect of growth rate on quartz defects: Journal of Crystal Growth, v. 62, p. 203–206.
Merino, E., 1984, Survey of geochemical self-patterning phenomena, *in* Nicolis, G. and Baras, F., editors, Chemical Instabilities: Boston, Reidel, p. 305–328.
Merino, E., Wang, Y., and Deloule, E., 1995a, Trace element content and the twisting of chalcedony fibers in agate: Geometry and microanalyses: American Journal of Science, under revision.
———— 1995b, Genesis of agates in flood basalts, and petrological implications: Geochimica et Cosmochimica Acta, to be submitted.
Michel-Lévy, A., and Munier-Chalmas E., 1892, Mémoire sur diverses formes affectées par le réseau élémentaire du quartz: Bulletin de la Société Française de Minéralogie, v. 15, p. 161–190.
Miehe, G., Graetsch, H., and Flörke, O. W., 1984, Crystal structure and growth fabric of length-fast chalcedony: Physics and Chemistry of Minerals, v. 10, p. 197–199.
Mitsyuk, B. M., 1974, Mechanism of hydrothermal synthesis of quartz: Geochemistry International, v. 11, p. 1151–1156.
Nacken, R., 1948, Über die Nachbildung von Chalcedon-Mandeln: Natur und Folk, v. 78, p. 2–8.
Nagy, K. L., and Lasaga, A. C., 1992, Dissolution and precipitation kinetics of gibbsite at 80°C and pH 3: The dependence on solution saturation state: Geochimica et Cosmochimica Acta, v. 56, p. 3093–3111.
Nicolis G., and Prigogine I., 1977, Self-organization in Non-equilibrium Systems: New York, Wiley, 491 p.
———— 1989, Exploring Complexity: An Introduction: New York, W. H. Freeman, 313 p.
Oehler, J. H., 1976, Hydrothermal crystallization of silica gel: Geological Society of America Bulletin, v. 87, p. 1143–1152.
Ortoleva, P., Chadam, J., Merino, E., and Sen, A., 1987, Geochemical self-organization II: The reactive-infiltration instability: American Journal of Science, v. 287, p. 1008–1040.
Pankrath, R., 1991, Polarized IR spectra of synthetic smoky quartz: Physics and Chemistry of Minerals, v. 17, p. 681–689.
Parks, G. A., 1984, Surface and interfacial free energies of quartz: Journal of Geophysical Research, v. 89, p. 3997–4008.
Raman, C. V., and Jayaraman, A., 1954, The structure and optical behaviour of iridescent agate: Proceedings of the Indian Academy of Sciences, v. A38, p. 199–206 + plates.
Rimstidt, J. D., and Barnes, H. L., 1980, The kinetics of silica-water reactions: Geochimica et Cosmochimica Acta, v. 44, p. 1683–1699.
Sekerka, R. F., 1973, Morphological instability, *in* Hartman, P., editor, Crystal Growth: An Introduction: Amsterdam, North-Holland, p. 403–443.
Sunagawa, I., and Ohta, E., 1976, Mechanism of formation of chalcedony: Science Reports of the Tohuku University, v. 13, p. 131–146.
Tritton, D. J., 1988, Physical Fluid Dynamics: New York, Oxford University Press, 519 p.
Walther, J. V., and Helgeson, H. C., 1977, Calculation of the thermodynamic properties of aqueous silica and the solubility of quartz and its polymorphs at high pressures and temperatures: American Journal of Science, v. 277, p. 1315–1351.
Wang, Y., and Merino, E., 1990, Self-organizational origin of agates: Banding, fiber twisting, composition, and dynamic crystallization model: Geochimica et Cosmochimica Acta, v. 54, p. 1627–1638.
———— 1992, Dynamic model of oscillatory zoning of trace elements in calcite: Double layer, inhibition, and self-organization: Geochimica et Cosmochimica Acta, v. 56, p. 587–596.
White, J. F., and Corwin, J. F., 1961, Synthesis and origin of chalcedony: American Mineralogist, v. 46, p. 112–119.